Acta Geologica Sinica (English Edition), 2023, 97(2): 486–500

Exhumation and Preservation of the Jinchuan Ni-Cu-PGE Deposit under the East Longshou Mountain Thermal Evolution, Revealed by Apatite Fission Track Thermochronology

LEI Xianghe[1], YU Qiang[1, 2, *], JIAO Jiangang[1, 2, 3], LIU Jian[4], SUN Xianyao[1], HE Lijuan[1] and YANG Qike[1]

[1] *School of Earth Science and Resources, Chang'an University, Xi'an 710054, China*
[2] *Key Laboratory of Western China's Mineral Resources and Geological Engineering, Ministry of Education, Chang'an University, Xi'an 710054, China*
[3] *Xi'an Key Laboratory for Mineralization and Efficient Utilization of Critical Metals, Xi'an 710054, China*
[4] *Department of Geology, Northwest University, Xi'an 710069, China*

Abstract: Uplift and exhumation are important factors affecting the preservation of deposits. The anatomy of uplift-cooling evolution and exhumation in the East Longshou Mountain is of significant research value in understanding changes in the Jinchuan Ni-Cu-PGE deposit since its formation. This study uses apatite fission track (AFT) thermochronology to reconstruct the thermal history of the East Longshou Mountain, including the Jinchuan mine, revealing the uplift and exhumation history of the East Longshou Mountain and elucidating the preservation status of the Jinchuan deposit. The AFT ages in the East Longshou Mountain are distributed from 62.3 ± 3.0 Ma to 214.7 ± 14 Ma, with significant differences in ages in distinct areas, the central and pooled ages being consistent within the margin of error. Inverse thermal history models reveal two rapid cooling events associated with exhumation from the Early Jurassic to the Early Cretaceous (200–100 Ma) and since the Miocene (15–0 Ma), the former attributable to the far-afield response to the closure of the Paleo-Tethys Ocean and plate assembly at the southern margin of Eurasia, the latter associated with the initial India-Eurasia plate collision. A slow cooling event from the Early Cretaceous to the Miocene (100–15 Ma) is thought to be related to the arid environment in northwest China since the Cretaceous. These cooling events have diverse responses and cooling rates in different blocks of the East Longshou Mountain: the southwest and centre of which are mainly cooled over 200–120 Ma and 120–0 Ma, with cooling rates of ~0.25 and ~0.33 °C/Ma (~1.25 and ~0.33 °C/Ma in the centre); the Jinchuan mine primarily cooled over 160–100 Ma, 100–15 Ma and 15–0 Ma, with cooling rates of ~1.33, ~0.25 and ~2.00 °C/Ma. These differentiated coolings imply that the uplift of the East Longshou Mountain before the Miocene (~15 Ma) was integral. Strong uplift then occurred in the vicinity of the mining area, which is a critical period for the uplift of the Jinchuan deposit to the surface, meaning that the Jinchuan deposit was exposed no earlier than the Miocene (~15 Ma). Based on mineralization depth information obtained by previous researchers, in conjunction with the calculation and simulation results of this study, it can be seen that the bulk of the Jinchuan intrusion may still be preserved at depth.

Key words: apatite fission track, deposit preservation, uplift-cooling, Jinchuan Ni-Cu-PGE Deposit, East Longshou Mountain

Citation: Lei et al., 2023. Exhumation and Preservation of the Jinchuan Ni-Cu-PGE Deposit under the East Longshou Mountain Thermal Evolution, Revealed by Apatite Fission Track Thermochronology. Acta Geologica Sinica (English Edition), 97(2): 486–500. DOI: 10.1111/1755-6724.15036

1 Introduction

The Jinchuan Ni-Cu-(PGE) sulfide deposit is the largest copper-nickel deposit in China and the third largest one globally. It contains more than 500 Mt of ore and accounts for 88% of Ni, 90% of PGE and 13% of Cu production in China, making it the largest Ni, Cu and PGE metal supply base in China (Chai and Naldrett, 1992; Tang et al., 1992; Naldrett, 1997; Zhang et al., 2004; Song X Y et al., 2009; Gao H et al., 2009). Due to the significance of the Jinchuan deposit in China, it has long been a focus for research. In the past, studies on the Jinchuan deposit have mainly focused on the genesis of the deposit, its diagenesis and mineralization, mineralization age, geochemical characteristics, mineralization temperature and pressure etc. (Wu et al., 1992; Xie et al., 1998; De Waal et al., 2004; Tang et al., 2014; Xiao et al., 2018; Jiao et al., 2019; Mao et al., 2019; Zhao et al., 2022). These studies did not focus on the changes and preservation of the deposit after mineralization.

Deposit preservation is considered to be an essential component of mineralization systems (Wyborn et al., 1994; Kesler and Wilkinson, 2006), Zhai et al. (2000) emphasizing that attention should be paid to deposit preservation and proposing that deposits could undergo a variety of degrees and styles of modification. Yuan (2016) argued that exploring the preservation conditions and distribution patterns of deposits in the later stages of mineralization, then discovering and predicting hidden

* Corresponding author. E-mail: yuqiang@chd.edu.cn

deposits can shed new light on further potential mineral exploration and prospecting. Sun et al. (2021) considered that post-mineralization uplift and exhumation should directly guide evaluation of deposit preservation and mineralization potential. Wang et al. (2008) contended that regional uplift and exhumation are the critical factors affecting the change and preservation of the deposit.

AFT thermochronology enables the reconstruction of upper crustal uplift cooling history in the temperature range ~110–60°C (Gleadow and Duddy, 1981; Reiners and Brandon, 2006), corresponding to a depth range of 2–4 km below the surface. Studying the thermal history above that depth can provide essential constraints on the regional uplift-exhumation history (Ehlers, 2005; Yu et al., 2019, 2021, 2022; Fan et al., 2021; Yang et al., 2021) and the deposit preservation (Deng et al., 2014; Liu X L et al., 2021). Thus, AFT thermochronology can be used to quantify the exhumation histories and timings of the metallogenic thermal events and has useful applications in mineral exploration (McInnes et al., 2005). Here, based on previous studies on the Jinchuan deposit and Longshou Mountain tectonic belt, this study explores the thermal evolutionary history of the East Longshou Mountain and the uplift and exhumation processes of the Jinchuan Mining Area since the Early Jurassic, using AFT thermochronology, with the objective of clarifying the thermal evolutionary history of the East Longshou Mountain and the preservational status of the Jinchuan deposit after mineralization.

2 Geological Setting

The Jinchuan world-class sulfide copper-nickel deposit is located in the Longshou Mountain uplift belt at the southwest margin of the Alxa Block, North China Craton, which is separated from the Qilian Fold Belt to the south by the South Margin Fault and liesadjacent to the Chaoshui Basin to the north at the North Margin Fault of the Longshou Mountain (Fig. 1a, b) (Chai and Naldrett, 1992; Naldrett, 1999; Gao Y L et al., 2009; Tang et al., 2014; Yu et al., 2020). The Paleoproterozoic Longshou Mountain Group dominates the basement of the Longshou Mountain Belt, the cover including Meso- and Neoproterozoic metamorphic sedimentary rocks. Along the Longshou Mountain, several mafic–ultramafic intrusions (groups) and medium–felsic intrusions extend about 200 km from east to west (Fig. 1b). The Longshou Mountain Belt mainly consists of Precambrian, Devonian, Carboniferous, Permian and Jurassic strata (Fig. 2b), of which the oldest rocks are oblique oblong amphibolite and granite gneisses of 1.9–2.7 Ga (Gong et al., 2012).

The Jinchuan intrusion intruded into the former Changcheng System Baijiazuizi Formation with a 10° cross-angle, which directly contacts dacite, mixed rock and gneiss, across an area about 6.5 km long, 20–500 m wide, extending downwards in a V-shape for more than 1100 m (Fig. 1c, d). The centre of the Jinchuan intrusion is exposed due to exhumation in a lens-shaped area of 1.34 km^2. The uplift area of the Longshou Mountain belongs to the intraplate rift environment (Zeng et al., 2013), the faults and joints being developed in the mining area. These faults strictly controlled the migration and deposition of ore-forming materials during the metallogenic period; after mineralization, the strong fracture activity destroyed the continuity of the intrusion controls. The main faults in the mining area include F_1, F_8, F_{17}, F_{23}, F_{16} and F_{16-1}. The Jinchuan intrusion is staggered by the NEE compressive-torsional fault and is divided into 4 sections. They are named III, I, II and IV (mining area) from west to east, according to the mining sequence (Fig. 1c, d). Among them, the three main ore bodies with proven reserves and great economic value are ore bodies #1 and #2 in II mining area and ore body #1 in I mining area (Fig. 1c, d). The Jinchuan copper-nickel sulfide deposits primarily develop three types of ore: massive sulfide ore, disseminated sulfide ore and net-textured sulfide ore (Fig. 1d), containing 5% to 20%, 25% to 40% and more than 70% sulfide, respectively. The most common sulfide combination of ore is magnetite-nickel-pyrite-chalcopyrite, the associated platinum group minerals including bismuth, telluride, selenide and arsenite platinum ore.

3 Materials and Methods

3.1 Sample collection

To systematically explore the thermal history of East Longshou Mountain, the team not only considered that the sampling points should fully control the tectonic belt of East Longshou Mountain, but also fulfilled the requirements of fission track thermal chronology for the altitude of the sampling point (in order to obtain more realistic data, different sampling points should maintain a certain altitude difference). Ultimately, the team developed three sampling routes from the study area's southwest rim to the northeast rim (Fig. 2a). A total of 36 fresh rock samples (Fig. 2a) were collected after field prospecting and practical considerations, with each sample having a mass of no less than 9 kg. However, during later sample processing, it was found that there were nine samples from which a single apatite grain could not be picked out, ten samples from which fewer than 500 single apatite grains could be picked out, with only 15 rock samples that had more than 500 single apatite grains. Ultimately, 13 samples were obtained for experiments, following later experimental processing. Analysis of the sampling topographic map shows (Fig. 2a, b) that although 23 rock samples could not participate in the experiment, the remaining 13 samples can still satisfy the sampling target set by the team, so the study could commence on the basis of these 13 samples. Specific information about the above 13 samples is shown in Table 1.

3.2 Analytical methods

The preparation of the samples and the gathering of statistics regarding the track density and confined track lengths were conducted at the State Key Laboratory of Continental Dynamics, Northwestern University, the ^{238}U content being tested at Beijing Kronen Technology Co. After the samples were crushed and ground, the apatite grains were sorted by conventional heavy liquid separation

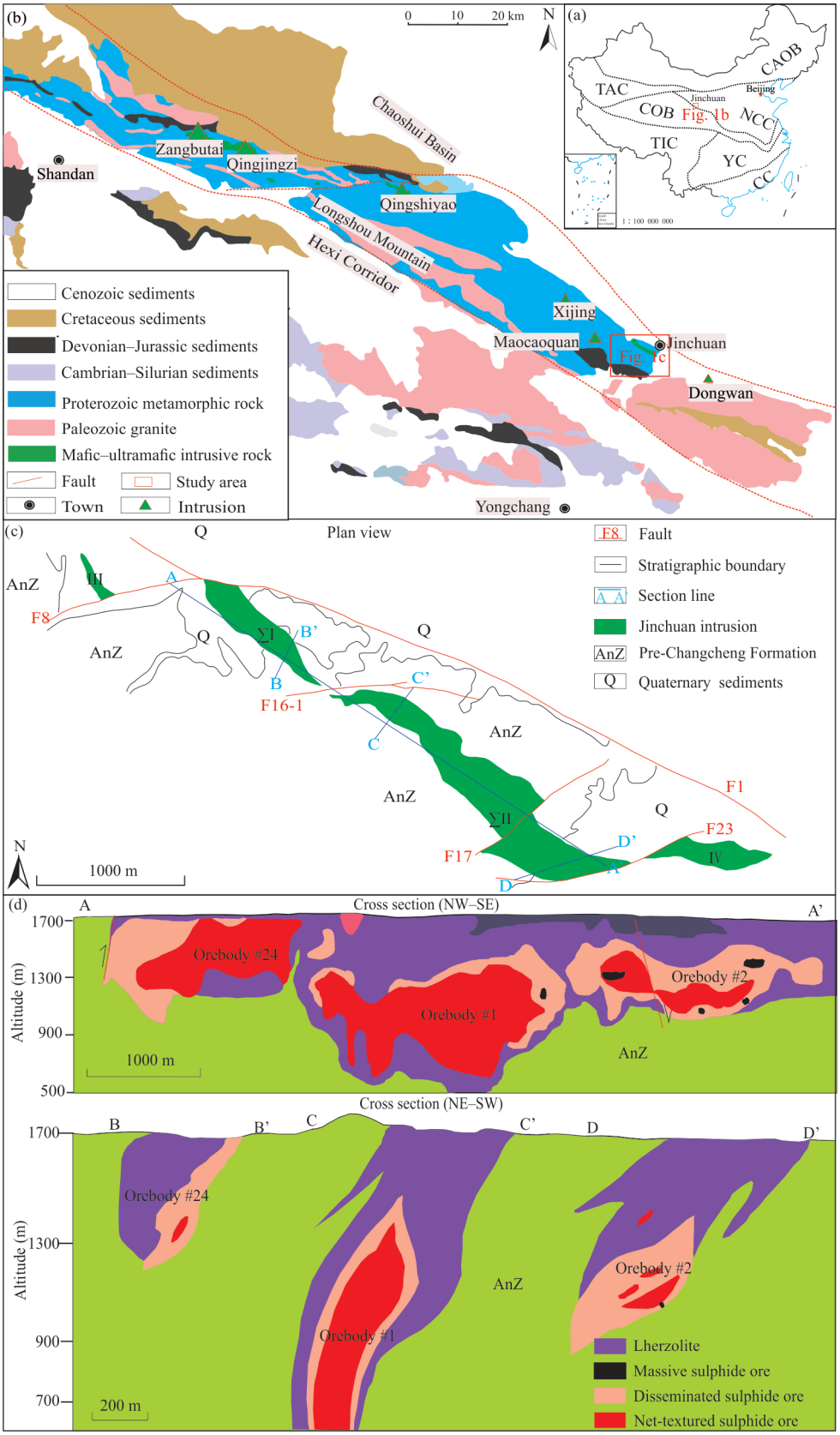

Fig. 1. (a) Location map (China basemap after China's National Bureau of Surveying and Mapping Geographical Information); (b) geological sketch of Longshou Mountain, the rectangular box indicates the study area shown in detail in (c); (c) plan view of the Jinchuan Mining Area; (d) cross-section of the Jinchuan Mining Area.

Abbreviations: CAOB = Central Asian Orogenic Belt; CC = Cathaysia Craton; COB = Central Orogenic Belt; NCC = North China Craton; TAC = Tarim Craton; TIC = Tibet Craton; YC = Yangtze Craton.

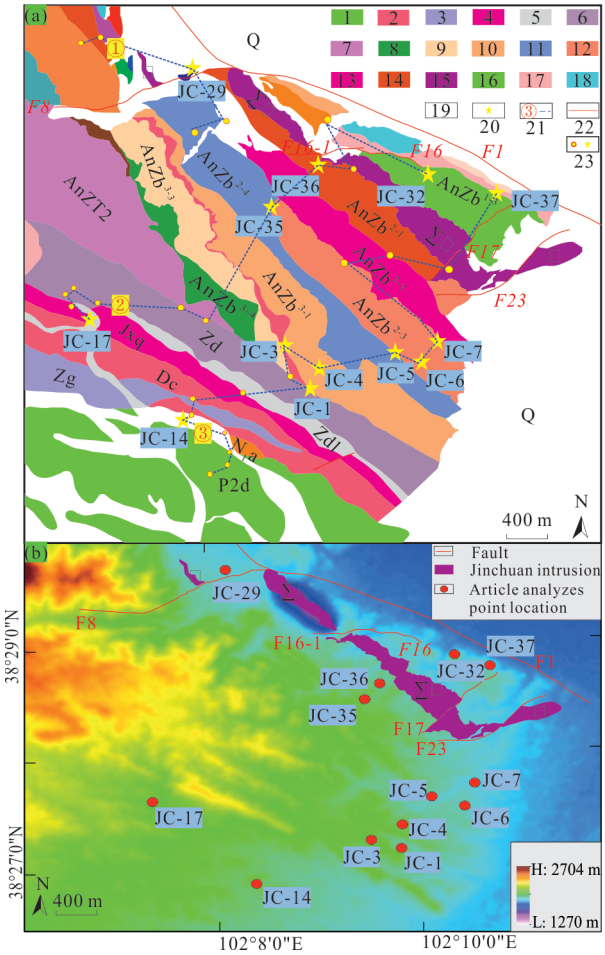

Fig. 2. (a) Stratigraphic distribution and sampling route map for East Longshou Mountain; (b) topographic map of East Longshou Mountain.

1–Glutenite; 2–purplish red siltstone; 3–grayish green sericite slate; 4–greenish gray metamorphic banded dolomite; 5–greenish gray gravelly sericite phyllite; 6–greenish gray dolomite; 7–sericite biotite quartz schist; 8–serpentine marble; 9–streak of homogeneous migmatite; 10–eclogite-bearing biotite gneiss; 11–serpentine marble; 12–eclogite-bearing biotite gneiss; 13–chlorite quartz schist; 14–streak of homogeneous migmatite; 15–ultrabasic rock; 16–serpentine marble; 17–biotite plagioclase gneiss; 18–breccia migmatite homogeneous migmatite; 19–Quaternary system; 20–AFT analysis point; 21–actual sampling route; 22–fault; 23–sampling point.

and magnetic separation methods. The selected apatite grains were spread on a polytetrafluoroethylene plate and then fixed on a slide with epoxy resin; after 24 h of curing, they were sanded and polished to expose the maximum inner surface area, In order to reveal spontaneous tracks and etch them with 5.5 mol/L HNO_3 for 20 s at room temperature (20 ± 0.5°C). The statistics of spontaneous track density and confined track lengths were counted under a Zeiss Axio Imager M2m microscope with Zeiss Axio vision analysis software. After microscopically counting the density of spontaneous tracks, the length of confined tracks and the Dpar (arithmetical mean of etch-pit lengths parallel to the crystallographic c-axis) for apatite grains with a uniform distribution of spontaneous tracks, the location where the ^{238}U content needs to be measured was circled and the apatite grains were located.

Table 1 Sample information location and lithology

Sample	Latitude	Longitude	Elevation (m)	Lithology	Crystalized era
JC-1	38°27'20"N	102°09'32"E	1722	Granite	$AnZb^{3-1}$
JC-3	38°27'21"N	102°09'29"E	1686	Gneiss	$AnZb^{3-2}$
JC-4	38°27'37"N	102°09'20"E	1610	Granite	$AnZb^{3-1}$
JC-5	38°27'44"N	102°09'49"E	1665	Granite	$AnZb^{2-1}$
JC-6	38°27'44"N	102°09'49"E	1665	Granite	$AnZb^{2-2}$
JC-7	38°27'39"N	102°10'22"E	1628	Gneiss	$AnZb^{2-3}$
JC-14	38°27'6"N	102°08'17"E	1696	Sandstone	P_2d
JC-17	38°27'47"N	102°07'25"E	1745	Sandstone	Dc
JC-29	38°29'31"N	102°08'33"E	1620	Granite	$AnZb^{2-1}$
JC-32	38°28'48"N	102°10'16"E	1597	Granite	$AnZb^{2-1}$
JC-35	38°28'36"N	102°09'09"E	1680	Gneiss	$AnZb^{2-3}$
JC-36	38°28'42"N	102°09'25"E	1659	Granite	$AnZb^{2-1}$
JC-37	38°28'46"N	102°10'59"E	1589	Granite	$AnZb^{1-1}$

The positioned apatite grains were measured at ^{238}U using LA-ICP-MS with a background acquisition signal of 20 s and a laser exhumation time of 20 s. Durango apatite was used as a secondary reference to assess the quality of the analysis, ICPMS DataCal software being used for data processing. The LA-ICP-MS fission-track age calculation principle is quoted from Hasebe et al. (2004), the relevant parameters coming from the Laboratory of Low-Temperature Thermochronology and Fission Tracks at the University of Melbourne, as follows:

$$t=\frac{1}{10^6\times\lambda_D}\ln(1+\lambda_D\xi\frac{\rho_a}{C_u})$$

where t: AFT age; λ_D: the total decay constant of ^{238}U, 1.55×10^{-10}; ρ_a: spontaneous track density; C_u: LA-ICP-MS tested at a concentration of ^{238}U; ξ: correction coefficient, 2080, which is equivalent to the zeta value of traditional methods, calculated as:

$$\xi=\frac{M}{\lambda_f N_A d R_{Ap} g q_{Ap}}$$

where M: the relative atomic mass of ^{238}U, 238.05 g/mol; λ_f: ^{238}U spontaneous fission constant, 8.46×10^{-17}; N_A: Avogadro's constant, 6.02×10^{23}; d: the density of apatite, 3.19 g/cm^3; R_{Ap}: the counting factor of spontaneous tracks that can be observed on a single particle profile, usually taking half of the average spontaneous fission track length, that is 7.5×10^{-4} cm; g: the experimental detection efficiency, 1; q_{Ap}: etch fact, 1. The formula for the age error σ_t of a fission track single particle is:

$$\sigma_t=t\sqrt{\frac{1}{N_s^2}+\sigma_u^2}$$

where N_s: the total spontaneous trace, σ_u: the uncertainty of the measured concentration of ^{238}U.

3.3 Calculation method of cooling rate

Cooling and exhumation rates are vital indicators for describing thermal history and are commonly calculated by mineral pair, thermal history modelling and age-closure temperature (Gunnell et al., 2003; Ding et al., 2007). The mineral pair method refers to dating minerals by different methods then using their ratio of closure temperature difference to relate to their age difference. The thermal

history modelling method is based on the modelling curve and the division of the cooling interval. The age-closure temperature method functions by assuming the regional geothermal gradient and uniting present surface temperature, ages and closure temperature, the equation being C_r (°C/Ma) = $(T_m - T_{surf})/t_m$ (Zeitler et al., 1982), where T_m, T_{surf} and t_m are the closure temperature, surface temperature and ages, respectively.

4 Results

4.1 Experimental data

The test results of 13 samples were obtained after crushing, gravity separation, magnetic separation, sample preparation, sectioning, track statistics, laser analysis and AFT age calculation, the results being shown in Table 2. Over 20 AFT ages and more than 50 confined track lengths were obtained for each sample, except for JC-7 and JC-35, for which only 11 age data and 12 confined track lengths were obtained. The AFT age data were detected by Radial Plotter software (Vermeesch, 2009) to test whether they belonged to the same age composition (Galbraith, 1990) and to obtain central ages and radial diagrams of single-grain ages (Fig. 3). The chi-square test results showed that except for the JC-7 sample with P(χ2) = 0, other samples passed the chi-square test, yielding P(χ2) values greater than 5% (Fig. 3). Moreover, this indicates that the AFT ages of all except JC-7 were composed of the same ages, representing the most recent cooling event; therefore, the pooled ages were used for each sample except for JC-7 (Galbraith and Laslett, 1993). The scattered AFT ages distribution of JC-7 may be related to the non-uniformity of ^{238}U concentration microzone test results during LA-ICP-MS measurements and other factors (Hasebe et al., 2004), so JC-7 was not considered in the subsequent discussion. The distribution of pooled ages is 214.7 ± 14 Ma to 62.3 ± 3 Ma, scattered but relatively closed in different study blocks, which can be divided into JC-14 and JC-17 (197 ± 10.2 Ma and 214.7 ± 14 Ma) at the southwest edge of the East Longshou Mountain, JC-(1-6) (135.4 ± 7.8 Ma to 98.7 ± 18 Ma) at the centre of the East Longshou Mountain and JC-(29-37) (81.7 ± 3.2 Ma to 62.3 ± 3 Ma) in the Jinchuan Mining Area. All AFT ages are significantly younger than their diagenetic ages, indicating that the rock samples might undergo thermal alteration or thermally reset after diagenesis, which reflects the fact that information on later cooling does not represent information on the source area. The mean track length (MTL) of all samples is 10.09–12.75 μm, with slight variations; the distribution of confined track lengths having a single-peak, slightly wide pattern, which suggests that the samples might have experienced a more complex thermal history or remained in the partial annealing zone for a particular period. Chang et al. (2004) concluded that the smaller the Dpar, the faster the annealing rate, the Dpar of all 13 samples being in the range 1.02–2.20 μm, indicating that the annealing resistance of the apatite samples in this study was limited.

4.2 Data interpretation

Numerous experiments and studies have shown that even apatite grains within the same rock have different annealing behaviour, which means that under the same geological conditions (temperature), different apatite grains exhibit different lengths and ages (Zhou and Donelick, 2001). Variations in Dpar values can point to composition-related annealing resistance between samples (Carlson et al., 1999; Donelick et al., 2005). There was no correlation between the single grain AFT ages and Dpar, ^{238}U content and MTL for this study (Figs. 3, 4, 5a), suggesting the AFT age dispersion between samples might be independent of apatite chemistry and ^{238}U measurements. In contrast, the moderately short MTL values, the slightly wide distribution of confined track lengths and the relatively remarkable dispersion distribution of single grain AFT ages (Table 2; Fig. 3) all mean that the samples underwent a complex thermal history, rather than the experimental results being caused by differences in chemical fractions between single apatite grains. If the East Longshou Mountain achieved uplift cooling as a single block and a moderate cooling rate is assumed, i.e., no large-scale geothermal advection, we can expect a general relationship between AFT ages and elevations (Feng et al., 2017). However, the correlation

Table 2 Results of AFT analysis

Sample	No. grains	ρ_s(*N*s) ($\times 10^6$/cm^2)	^{238}U (ppm ± 1σ)	AFT age (Ma ± 1σ)	P(χ2) (%)	Central age (Ma ± 1σ)	MTL (μm)	No. tracks
JC-1	20	11.3(168)	17.77 ± 0.66	132 ± 15.1	19.00	135.0 ± 13	12.02	53
JC-3	21	4.37(138)	4.45 ± 0.41	127.1 ± 15.3	81.00	121.0 ± 10	13.32	51
JC-4	24	17.88(233)	21.48 ± 0.7	135.4 ± 7.8	78.00	140.1 ± 9.6	12.4	101
JC-5	35	17.78(217)	39.02 ± 3.42	98.7 ± 5.5	68.00	102.5 ± 5.0	12.29	90
JC-6	21	7.38(134)	14.7 ± 0.82	101.2 ± 11.7	58.00	103.8 ± 9.2	11.92	59
JC-7	11	63.85(63)	6.38 ± 0.21	200.6 ± 57.3	0	233.4 ± 36.3	12.37	50
JC-14	28	23.47(210)	24.69 ± 0.78	197 ± 10.2	69.00	196.0 ± 14.0	11.55	88
JC-17	26	33.09(164)	31.12 ± 0.97	214.7 ± 14	82.00	224.0 ± 18	10.78	79
JC-29	24	17.48(294)	50.68 ± 2.45	71.9 ± 7	15.00	71.1 ± 4.8	10.96	68
JC-32	33	82.85(334)	17.24 ± 0.65	62.3 ± 3	42.00	88.4 ± 4.4	12.07	50
JC-35	20	11.47(116)	37.01 ± 2.97	71.7 ± 10.8	16.00	76.6 ± 9.5	12.64	12
JC-36	21	11.23(176)	28.97 ± 1.58	79.8 ± 5.6	86.00	82.4 ± 6.4	11.71	56
JC-37	28	29.52(231)	81.7 ± 3.2	83.1 ± 5.5	87.00	81.4 ± 5.5	10.09	94

No. grains: number of apatite crystals analyzed; ρs (*N*s): spontaneous fission-track density (number) of apatite crystals analyzed from samples; ^{238}U: uranium-238 concentration of samples measured by LA-ICP-MS, with absolute ± 1σ error value; P(χ2): chi-squared probability; AFT age–pooled ages, with absolute ± 1σ error ages; MTL–mean confined fission-track length of samples; No. tracks–number of apatite fission track analyzed.

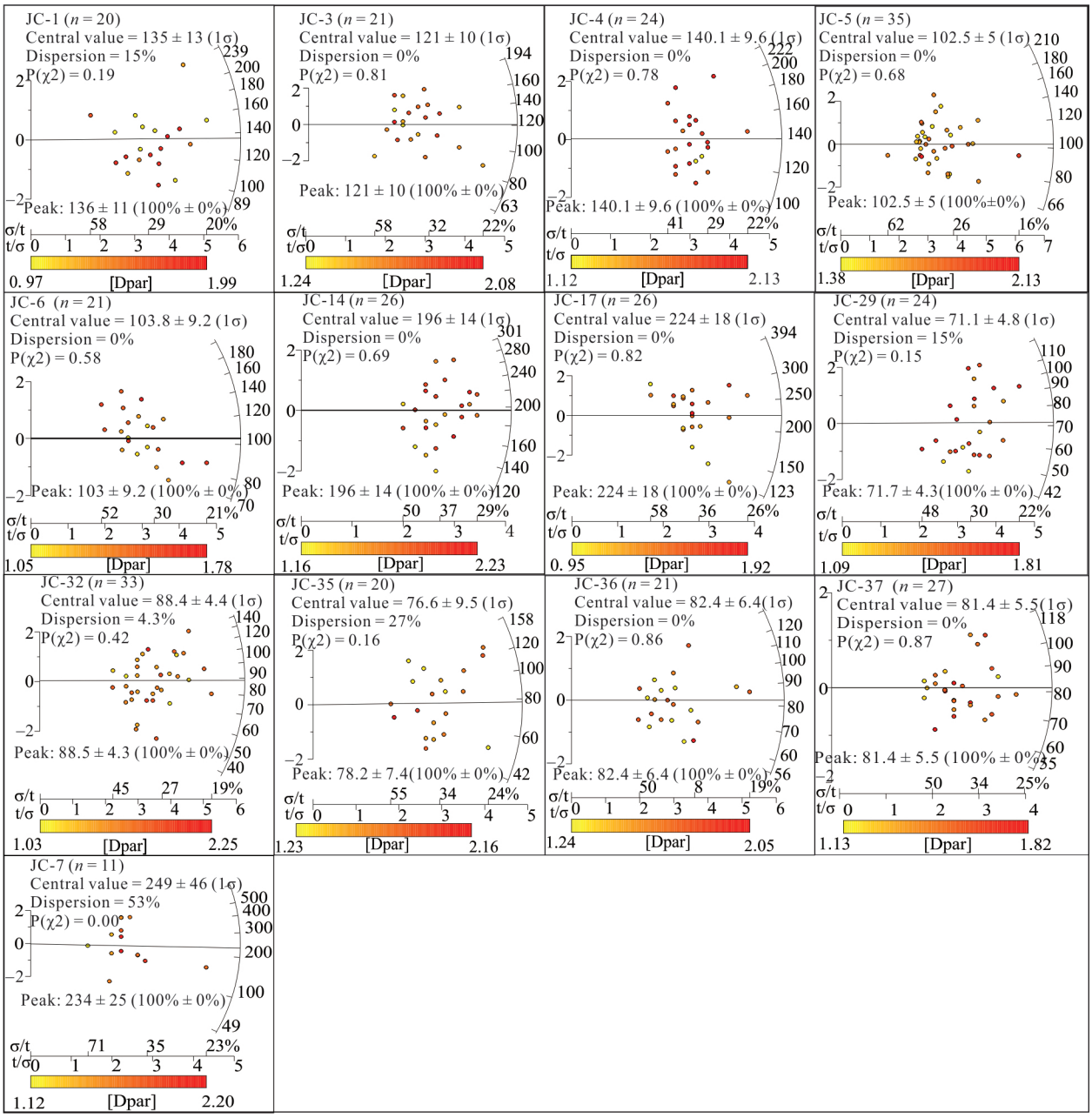

Fig. 3. The radial plot of fission-track ages of sampled apatites.

The AFT age for each point on a radial plot is obtained by projecting a line from the origin through the single-grain age (circles) to the radial axis. All points have the same size error bar corresponding to the axis about the origin on the left, showing ± 2σ. The further a point plots to the right of the origin, the more precise the individual grain age, as seen by the horizontal precision axis directly below the plot. The color assigned to each individual point shifts from yellow to red with increasing Dpar (μm).

between the AFT ages and the current samples' elevations (Fig. 5b) varies between blocks, denoting differences in uplift processes in the East Longshou Mountain.

4.3 Inverse thermal history modelling

To quantify the thermal history recorded by thermochronological data, inverse thermal history modelling was performed, relying on a multivariate annealing model (Ketcham et al., 2007) and HeFTy (version v1.8.0), combining AFT ages with kinetic parameters, Dpar values and confined track lengths. The results are shown in Fig. 6. The initial conditions of the modelling are set as follows: (1) all samples are assumed to have undergone a monotonic cooling process (Lin et al., 2011); (2) the number of confined track lengths operated for the modelling is no less than 50, the confidence of the models being higher if the number of lengths is greater than 100 (Ketcham, 2005; Zhu et al., 2007); (3) the temperature of the AFT partial annealing zone (PAZ) is ~60–110°C (Gleadow, 1981); (4) the high *t*-*T* constraint for metamorphic rocks is set at no less than 160°C, which is about 50% earlier than the AFT ages (Ketcham et al.,

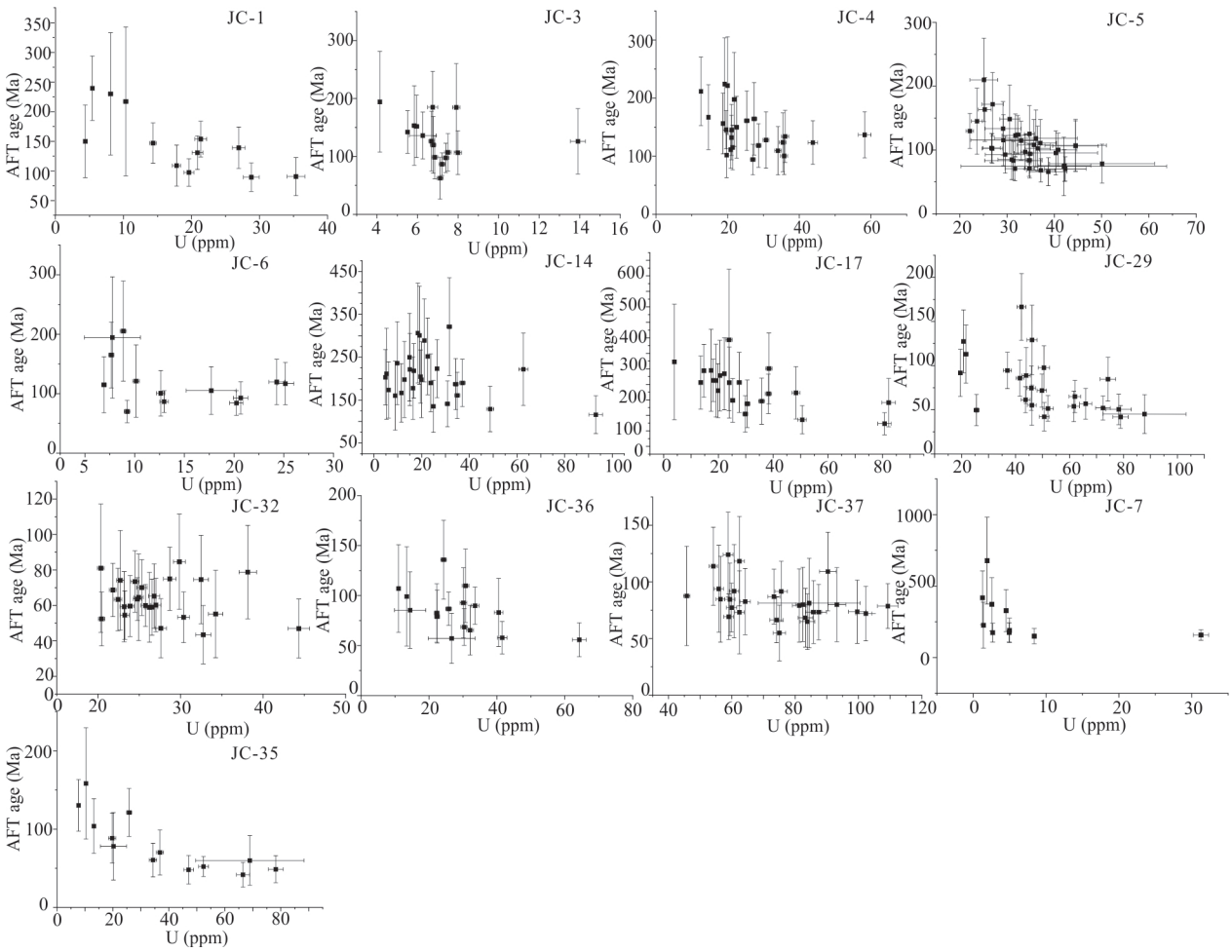

Fig. 4. ^{238}U content about single grain AFT age.
U, uranium-238 concentration of samples measured by LA-ICP-MS, with absolute ±1σ error value.

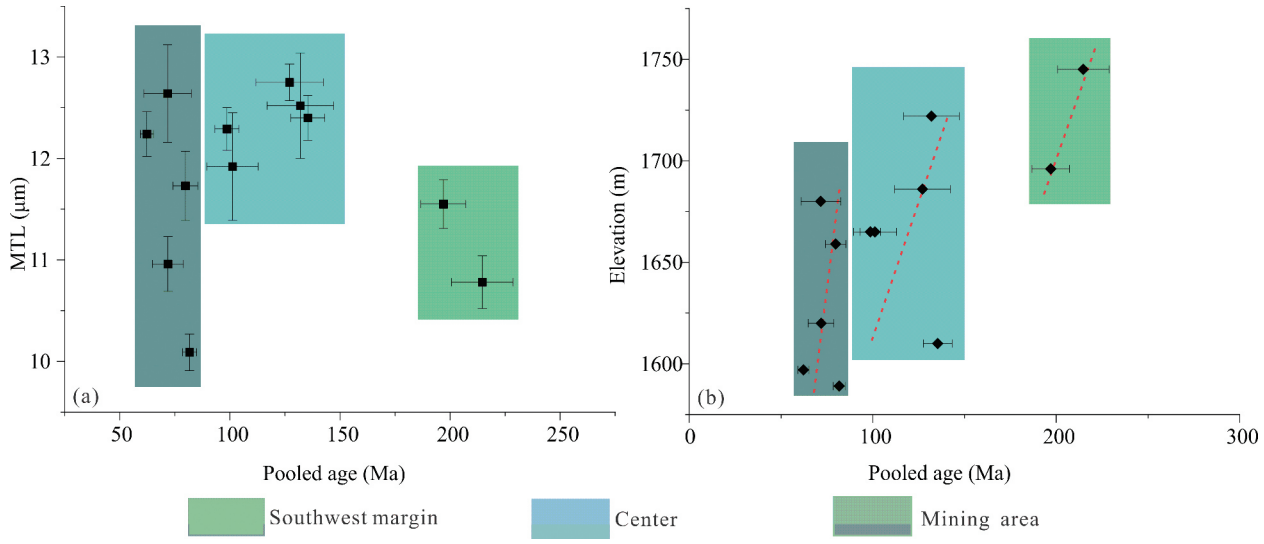

Fig. 5. Relationship between sample AFT age and elevation, MTL.
MTL = mean confined fission track length of samples; Southwest margin = southwest margin of the East Longshou Mountain; Mining area = the Jinchuan mining area.

2000); (5) the models were tested using the goodness-of-fit parameter (GOF), the results being acceptable for GOF > 0.05 and good for GOF > 0.5, as the larger the GOF value, the higher the confidence in the models (Ketcham,

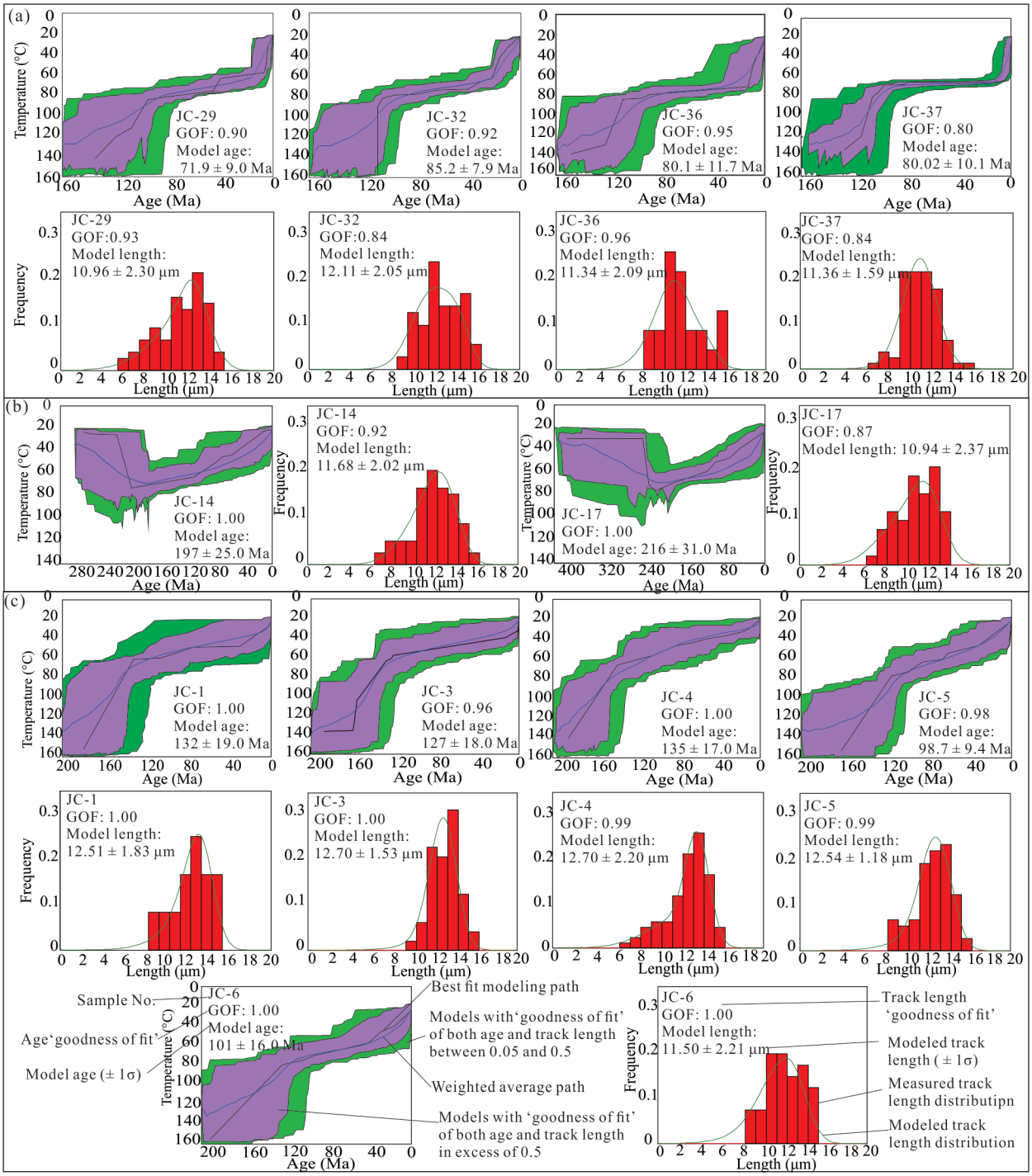

Fig. 6. Inversion thermal history modelling curves.
(a–c) Represent the thermal history modelling maps and related fitting parameters of the Jinchuan mine, southwest edge of the East Longshou Mountain and central part of the East Longshou Mountain, respectively.

2005); (6) each modelling path was set to 10,000. JC-35 does not participate in this modelling, because its confined track length data is less than 50, rendering the modelling not credible.

Eleven samples participated in the modelling, all giving plausible results, all models reproducing the AFT ages and confined track length distribution within the error limits. These thermal histories are all observed in the temperature interval with the AFT PAZ, which indicates that the modelling is well constrained (Fig. 6). JC-14 and JC-17 in the southwest margin of the East Longshou Mountain began cooling from the interior of the PAZ in the Early Jurassic until the Early Cretaceous relatively rapid cooling to the lower limit of the PAZ (~60°C); they mainly underwent a slow uplift from the Early Jurassic (~200 Ma) to the Early Cretaceous (~120 Ma) and a relatively rapid

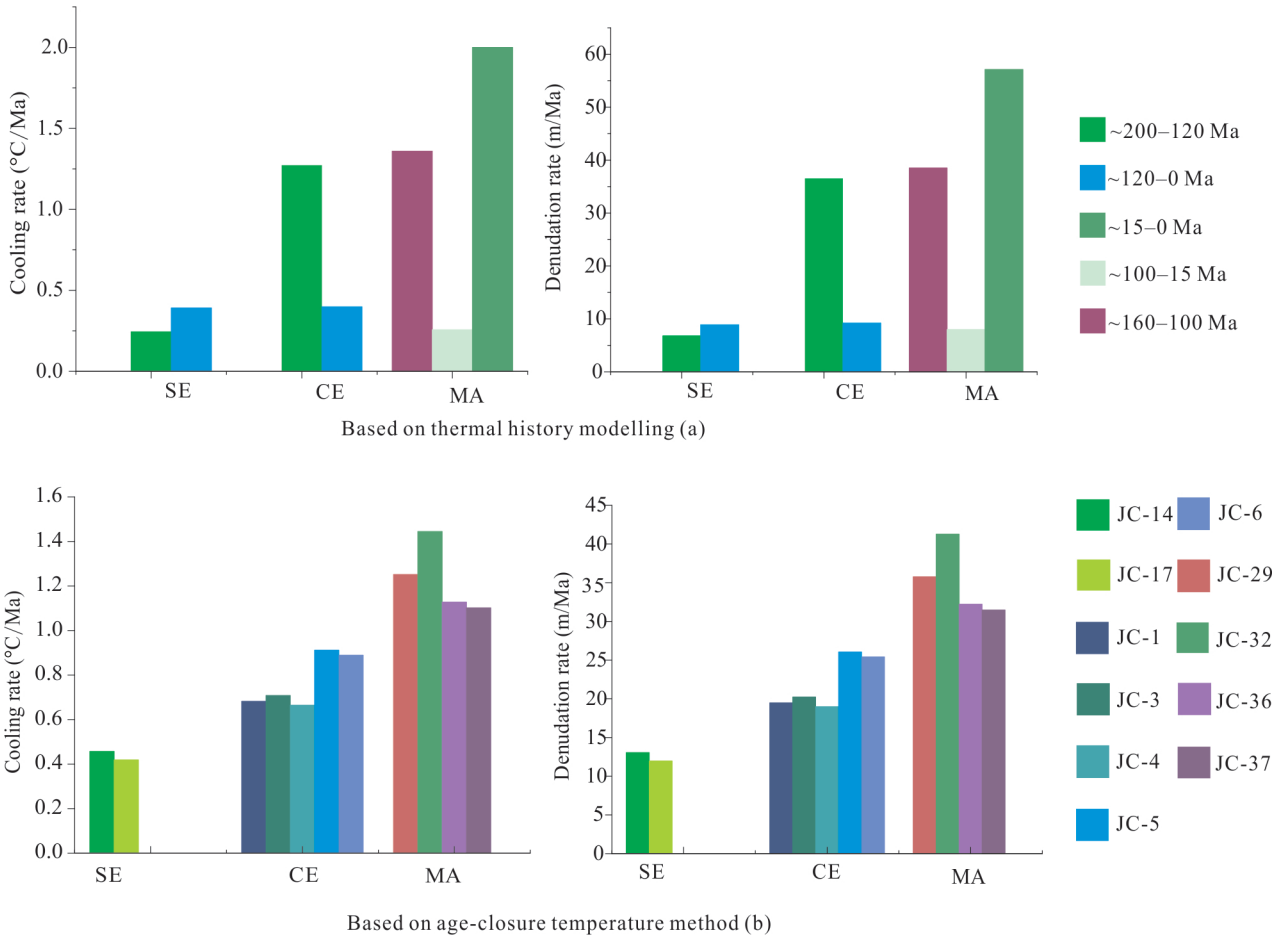

Fig. 7. (a) Thermal history modelling method and (b) age-closure temperature method used to calculate cooling and spalling rates. Abbreviations: SE = Southwest margin of the East Longshou Mts.; CE = Central East Longshou Moutain.; MA = Jinchuan mining area.

uplift since the Early Cretaceous (~120 Ma) (Fig. 6b). JC-(1–6) in the centre of the East Longshou Mountain cooled from above the upper PAZ (~110°C) in the Early Jurassic until the lower PAZ (~60°C) in the Early Cretaceous; they mainly experienced rapid uplift from the Early Jurassic (~200 Ma) to the Early Cretaceous (~120 Ma) and a slow uplift that has continued since the Early Cretaceous (~120 Ma) (Fig. 6c). The Jinchuan Mining Area (samples JC-29, JC-32, JC-32 and JC-37) cooled from above the upper PAZ limit (~110°C) in the Late Jurassic until the lower PAZ limit (~60°C) in the early Miocene; the mining area went through three stages of cooling: rapid uplift cooling from the Late Jurassic (~160 Ma) to the early Late Cretaceous (~100 Ma), which cooled the samples to 80°C; the tectonic smoothing period from the early Late Cretaceous (~100 Ma) to the Miocene (~15 Ma), which cooled the samples from 80°C to 60°C; and the relatively rapid uplift phase since the Miocene (~15 Ma), during which the samples were exposed from 60°C to surface temperature (~20°C) (Fig. 6a).

4.4 Cooling rate

In this study, the cooling and exhumation rates of the East Longshou Mountain were obtained, using the technique of thermal history modelling and age-closure temperature, where T_m and T_{surf} were taken as 110°C (Gleadow and Duddy, 1981) and 20 ± 5°C; based on previous studies of the region (Ren, 1998; Yu et al., 2018), a geothermal gradient of 35 °C/km being assumed, the results being shown in Fig. 7. The results obtained by the two methods are close to each other. The thermal history modelling method (Fig. 7a) shows that the cooling and exhumation rates in the centre and south of the Eastern Longshou Mountain are lower than the Jinchuan Mining Area. The age-closure temperature method (Fig. 7b) shows that the cooling and exhumation rates in the East Longshou Mountain have an increasing trend from south to north, the cooling rates and the degree of exhumation not being consistent throughout the Jinchuan Mining Area.

5 Discussion

5.1 Rock uplift and exhumation

Rock uplift is the behaviour of rock near the surface under internal dynamic geological action, whereas rock exhumation is the destruction of rock by external dynamic geological action. The relationship between rock uplift and exhumation, which is related to the geodetic level or paleo-elevation, can be expressed as $U = D + \Delta H + \Delta s.l$, where U and D are the thickness of rock uplift and exhumation,

ΔH is the difference between present surface elevation and paleo-elevation, and $\Delta s.l$ representing the magnitude of sea-level change (England and Molnar, 1990). Previous researchers believed that the present altitude of Longshou Mountain is the result of Cenozoic tectonic movements (Zhang, 1992; Yuan et al., 2013; Zhuang et al., 2018), the Mesozoic altitude of East Longshou Mountain therefore being assumed to be 500 m. For the AFT, $D + \Delta s.l$ is equivalent to the depth of burial corresponding to the AFT closure temperature, which gives $D + \Delta s.l$ = 3143 m and uplift rate = uplift amplitude/uplift year. The calculation of exhumation thickness is based on the formula proposed by Brown (1991): $\Delta E = (110 \pm 10 - T_s)/G + d$, or exhumation rate = exhumation thickness/exhumation year, where ΔE, T_s, G and d are exhumation thickness, paleosurface temperature, paleothermal gradient and the difference between the elevation of the AFT annealing zone at the bottom and the present surface. According to the research (Song C H et al., 2009) on the environment and climate of the northern margin of the Qinghai Tibet Plateau, T_s was assumed to be 30°C. The results of uplift and exhumation thickness since the AFT ages are shown in Table 3: the uplift thickness, uplift rate, exhumation thickness and exhumation rate are concentrated in 4232–4388 m, 20.438 –68.058 m/Ma, 3684 m–3840 m and 17.157–61.504 m/ Ma, respectively. It is possible that the initial topography was relatively gentle, the present landform being formed after uplift and exhumation (Yuan et al., 2011).

Table 3 Thickness rock uplift and exhumation

Block	Sample	Elevation (m)	U (m)	Uplift rate (m/Ma)	ΔE (m)	Denudation rate (m/Ma)
Southwest margin of the East Longshou Mountain	JC-14	1696	4339	22.025	3733	18.948
	JC-17	1745	4388	20.438	3684	17.157
Center of the East Longshou Mountain	JC-1	1722	4365	33.068	3707	28.081
	JC-3	1686	4329	34.060	3743	29.447
	JC-4	1610	4253	31.411	3819	28.203
	JC-5	1665	4308	43.647	3764	38.133
	JC-6	1665	4308	42.569	3764	37.191
The Jinchuan Mining Area	JC-29	1620	4263	59.291	3809	52.972
	JC-32	1597	4240	68.058	3832	61.504
	JC-36	1659	4302	53.910	3770	47.240
	JC-37	1589	4232	51.799	3840	46.998

U–uplift thickness; ΔE–denudation thickness.

5.2 Tectonic evolutionary history of the Longshou Mountain

The geological evolution of the Longshou Mountain, an important metallogenic belt in the interior of East Asia (Zhang, 1992; Zhao et al., 1994; Tang and Bai, 2000; Liu, et al., 2020; Liu W H et al., 2021), can be divided into the following stages: (1) the mantle upwelling at the end of the early Proterozoic caused the crystallization of the Paleogene boundary; meanwhile, the Alxa Block rose, resulting in intermittent sedimentation and the absence of the Changcheng System (Zhang, 1992; Tang and Bai, 2000); (2) the strong mantle activity in the middle Proterozoic caused the lateral extensional fracture to evolve into the Rift Sea (Zhao et al., 1994; Lu et al., 2018); (3) in the Neoproterozoic, the ancient Rift Valley opened along the southern boundary to form the North Qilian Ocean domain, while the Rift Valley zone was uplifted and connected with the Alxa Block; (4) in the early Paleozoic, a passive land margin was formed along the middle–eastern part of the Rift Valley zone; (4) in the early early Paleozoic, a passive terrestrial margin zone was formed along the southern margin of the rift zone, while in the late early Paleozoic, the rift zone was influenced by the collision of ancient plates and magma again invaded; (5) in the late Paleozoic, some original tensional fracture activities in the rift valley formed a fractured sea trough and deposited some land surface marine clastic rocks and carbonates (Zhang, 1992).

The tectonic evolution of the Longshou Mountain since the Mesozoic is characterized by its complexity. Li et al. (2020) tested apatite (U-Th)/He for Longshou Mountain near Taohuala Mountain and found that the northern flank of Longshou Mountain is older than the southern flank. Thermal history models revealed strong fracture activity on the southern flank of Longshou Mountain and weaker activity on the northern flank, with the Longshou Mountain as a whole showing a lift-slope pattern since the Miocene (~14 Ma); Zhang B H et al. (2017) used AFT data to model the thermal history of Dongda Mountain in the central Longshou Mountain and found that Dongda Mountain experienced two uplift events during ~130–25 Ma and since the late Cenozoic (~5 Ma); Wu et al. (2021) analyzed the AFT of the Longshou Mountain from Shandan County to the Jinchuan and the AFT ages were distributed between 95 ± 6 Ma to 26 ± 5 Ma. Thermal history models of some samples showed that Longshou Mountain has undergone multiple phases of complex exhumation processes since the late Mesozoic; in addition, related researchers have conducted AFT and zircon fission track (ZFT) tests for Jinchuan (Ma et al., 2014; Tian et al., 2016; Liu et al., 2022) and found that the AFT and ZFT ages are close. The above findings show that the Longshou Mountain region's uplift is not monolithic, the uplift time and exhumation degree differing from west to east. The close dating results of the AFT and ZFT of the same sample indicate that intense uplift may have caused it to cross the ZFT and AFT complete annealing zones simultaneously over a short period of time since the Cenozoic in Jinchuan.

This study demonstrates that the uplift of the East Longshou Mountain from south to north also differs. The AFT ages tend to decrease from south to north, implying that the southern part of the East Longshou Mountain broke away from the AFT complete annealing zone earlier than the northern part. Thermal models reveal the thermal history of the East Longshou Mountain (Fig. 6): the centre and south of East Longshou Mountain were the first parts to start uplifting during the Early Jurassic to Early Cretaceous (~200–120 Ma), which largely removed the central and southern parts from the partial annealing zone. The uplift of the Jinchuan Mining Area lagged behind the centre and southern part and happened during the Late Jurassic to Late Cretaceous (~160–100 Ma), which removed the mining area from the complete annealing zone and entered the partial annealing zone. This uplift coincided with the closure of the Paleo-Tethys Ocean and the assembly of Qiangtang Block at the southern margin of Eurasia and thus may be a far-afield reflection of these

events (Dewey et al., 1988; Chen et al., 2003). During the Late Cretaceous to Miocene period (~100–15 Ma), East Longshou Mountain was in a relatively smooth tectonic environment, with no violent tectonic movements. The cooling exhumation during this period may be related to the arid environment in northwest China since the Late Cretaceous (Xiang et al., 2015). The Jinchuan Mining Area has been dramatically uplifted since the Miocene (~15 Ma), leaving the south–central part unaffected. Although the modelling results occur between 0–60°C (Fig. 6a) with low confidence, there are similar traces of tectonic movements around the study area: Li et al. (2018) found that rapid denudation associated with the Haiyuan strike-slip fault occurred in the North Qilian area between 15–8 Ma; Zheng et al. (2017) and Wang et al. (2014) demonstrated that the North Qilian area started to recoil around 10 Ma; Zhang et al. (2009) considered that the North Margin Great Fault—F_1 (Fig. 2) underwent right-slip after the Miocene, so the modelling results are considered to be plausible. Based on the above, a hypothesis has been made that the East Longshou Mountain was retrogradely thrust since the Miocene (~15 Ma), bounded by the North Margin Fault, which coincides with the exhumation of the North Qilian Mountain since the Miocene and is considered to be a direct far-afield deformation response of the northeastern margin of the Tibetan Plateau to the initial Indo-Eurasian collision (George et al., 2001; Li et al., 2018; An et al., 2020).

The above analysis reveals that the East Longshou Mountain experienced a fierce uplift from the Early Jurassic to the Early Cretaceous, which caused the Jinchuan Mining Area to exit the complete annealing zone in the Late Jurassic. After the end of the uplift in the central and southern parts of the East Longshou Mountain since the Early Cretaceous, uplift still existed in the Jinchuan Mining Area on a certain scale until the early Late Cretaceous. Since then, the East Longshou Mountain has been in a stable environment except for the Jinchuan Mining Area, where a new phase of uplift has occurred since the Miocene.

5.3 Thermal history of the Jinchuan intrusion

Previously, it was thought that the Jinchuan intrusion formed in the Mesoproterozoic (1508 ± 31 Ma) (Tang et al., 1992); however, recently, the crystallization age of the Jinchuan intrusion was measured at ~830 Ma by zircon U-Pb (Li et al., 2005; Zhang et al., 2010) and the ~830 Ma mineralization age was also determined by using the Re-Os isotope system (Yang et al., 2005, 2008). The gabbro veins running through the Jinchuan intrusion and the anorthosite granites in the Jinchuan area were later dated to ~420 Ma by zircon U-Pb, so it is therefore hypothesized that the Jinchuan intrusion may have experienced a phase of thermal disturbance during the early Paleozoic (~420 Ma) (Duan et al., 2015; Zeng et al., 2016). Here, we combine published data (Table 4) and synthesize it with this study in order to constrain the thermal history of the Jinchuan intrusion since its mineralization and give possible thermal evolutionary paths a and b (Fig. 8). Path a (Fig. 8) is adapted from Ma et al. (2014), which combines the dating results of isotopic systems such as K-Ar, Rb-Sr, Sm-Nd and zircon U-Pb, AFT and ZFT to constrain the thermal history of the Jinchuan intrusion. In doing so, where the same isotopic systems showed different dating results, their credibility was reduced.

Path b (Fig. 8) utilizes zircon U-Pb, ZFT and AFT test results to constrain the thermal history of the Jinchuan intrusion: it formed in a tensional environment caused by

Table 4 Zircon U-Pb, ZFT and AFT ages at the Jinchuan mine

Sampling	Test items	Result (Ma)	Source
II-mining area	Zircon U-Pb	825	Li et al., 2005
I-mining area	Zircon U-Pb	831.8 ± 0.6	Zhang et al., 2010
II-mining area	Zircon U-Pb	420.6 ± 3.1 423.5 ± 1.4	Duan et al., 2015
II-mining area	Zircon U-Pb	433.4 ± 3.7, 361.7 ± 4.6	Zeng et al., 2016
West of F8	AFT, ZFT	105.56–51.53, 130.51–62.09	Tian et al., 2016
Mining area	AFT, ZFT	109 ± 8 to 68 ± 7 102 ± 11 to 68 ± 7	Ma et al., 2014

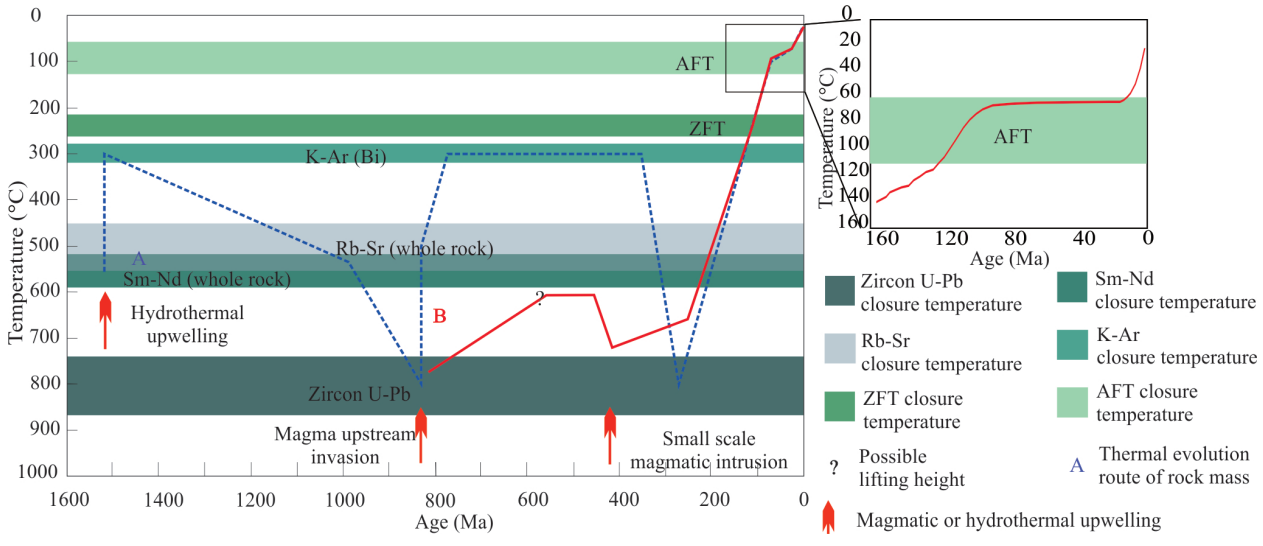

Fig. 8. Schematic diagram of the thermal evolution of the Jinchuan rock body since mineralization.

the rifting of the Rodinia supercontinent in the Neogene (~830 Ma) (Li et al., 2005; Zhao and Cawood, 2021) or was associated with the formation of the South China mantle column (Li et al., 1999); along with the continued rifting of Rodinia, the Jinchuan intrusion was uplifted continuously and it is speculated that the uplift stopped at the end of the Neoproterozoic with the completion of the rifting of Rodinia (Meert and Torsvik, 2003). The collision between the Alxa Block and the Qilian–Qaidam Block led to the upwelling of soft fluvial material, creating the Jinchuan intrusion warming in the Silurian (~420 Ma) (Zhang L Q et al., 2017). Since the Mesozoic (~200 Ma), influenced by the closure of the Paleo-Tethys Ocean, the Longshou Mountain has entered an overall uplift phase, the Jinchuan intrusion being cooled by the regional uplift (Kang et al., 2018). During the Cenozoic, the Jinchuan intrusion was remotely impacted by the India-Eurasia plate collision and was lifted to the surface to experience exhumation. Therefore, it can be inferred that the long-established Jinchuan intrusion started to be lifted from depth around the Mesozoic and was not exposed to the surface prior to the Miocene (~15 Ma), as it suffered from exhumation no earlier than the Miocene (~15 Ma).

5.4 Implications for Ni-Cu-PGE ore exploration

Studying the post-formation thermal history of the Jinchuan intrusion is key to evaluating its preservation. Thermal history models indicate that the East Longshou Mountain has been undergoing dramatic uplift since the Early Jurassic, while the south-central part of the East Longshou Mountain has been a tectonic plateau since the Early Cretaceous and the Jinchuan Mining Area has been experiencing strong uplift since the Miocene. Formerly, it was considered that the Jinchuan intrusion was pushed to the surface by means of pushover tectonics after deep mineralization (Shi et al., 1995; Gao H et al., 2009) and this study demonstrates that such pushover movements still existed since the Miocene and had a more muscular impact on the intrusion. Constraining the thermal history of the Jinchuan intrusion using dating data (Fig. 8) indicates that it was in a high-temperature environment until the Mesozoic, after which it began to cool from a high-temperature to a medium–low-temperature environment, violent movements since the Miocene lifting it to the surface. Calculations (Table 3) show that the uplift and exhumation thickness of the Jinchuan Mining Area since the Late Cretaceous is ~4 km and that of the East Longshou Mountain has been ~4 km since the Early Jurassic. The thermal models (Fig. 6) indicate that the initial uplift of the Jinchuan Mining Area began before the early overall uplift of the East Longshou Mountain was completed, suggesting a partial temporal overlap between the two uplifts and, therefore, the amount of exhumation of the Jinchuan Mining Area since the Mesozoic is known to be no greater than 8 km. Yang et al. (1991) studied the magma inclusions in the Jinchuan intrusion and concluded that the primary mineralized depth is ~10 km, so it can be seen that most of the ore body is still preserved at depth. The calculations (Table 3) also show that the uplift and exhumation near samples JC-29, JC-32 and JC-37 are similar, while the uplift is larger and the exhumation is smaller near sample JC-36. Therefore, from the perspective of deposit uplift and exhumation, this demonstrates a higher chance of finding the hidden ore body at the junction of mine areas I and II (Fig. 2b), where sample JC-36 is located.

6 Conclusions

(1) There have been differences in uplift since the Early Jurassic in the East Longshou Mountain. The south–central part of the East Longshou Mountain mainly experienced a rapid cooling from 200–120 Ma; the Jinchuan Mining Area experienced two rapid coolings from 200–100 Ma and 15–0 Ma; the East Longshou Mountain as a whole was in a tectonically stable period over 100–15 Ma.

(2) The Jinchuan deposit was exposed to the surface by thrust from the Miocene (~15 Ma) onwards, which is the critical period when the Jinchuan deposit was lifted to the surface, indicating that it has not been exhumed for a long time, compared to the mineralization era.

(3) The exhumation thickness of the northeast of East Longshou Mountain, represented by the Jinchuan deposit, since the Mesozoic is less than 8 km, which, combined with the depth of mineralization, indicates that most of the intrusion is still retained at depth. The junction of mine areas I and II in Jinchuan has a large amount of uplift, but small exhumation thickness, making the area favourable for mining exploration for preserved deposits.

Acknowledgments

We thank Prof. YAN Haiqing and the State Key Laboratory of Continental Dynamics of Northweste University for their help in this study. At the same time, we are also very grateful to the two anonymous reviewers and the editors for their valuable suggestions. This study was jointly funded by the National Natural Science Foundation Project (Grant No. 92162213), The Fundamental Research Funds for the Central Universities, CHD (Grant No. 300102272205).

Manuscript received Apr. 15, 2022
accepted Jan. 10, 2023
associate EIC: CHI Guoxiang
edited by Jeffery J. LISTON and FANG Xiang

Reference

An, K.X., Lin, X.B., Wu, L., Yang, R., Chen, H.L., Cheng, X.G., Xia, Q.K., Zhang, F.Q., Ding, W.W., Gao, S.B., Li, C.Y., and Zhang, Y., 2020. An immediate response to the Indian-Eurasian collision along the northeastern Tibetan Plateau: Evidence from apatite fission track analysis in the Kuantan Shan–Hei Shan. Tectonophysics, 774: 228278.

Brown, R.W., 1991. Backstacking apatite fission-track stratigraphy: A method for resolving the erosional and isostatic rebound components of tectonic uplift histories. Geology, 19(1): 74–77.

Carlson, W.D., Donelick, R.A., and Ketcham, R.A., 1999. Variability of apatite fission-track annealing kinetics. American Mineralogist, 84(9): 1213–1223.

Chai, G., and Naldrett, A.J., 1992. Characteristics of Ni-Cu-PGE mineralization and genesis of the Jinchuan Deposit, Northwest China. Economic Geology, 87(6): 1475–1495.

Chang, Y., Liu, R., and Yang, J., 2004. The summarization of fission-track technology and its applications in earth science. Shanghai Land and Resources, (1): 47–53 (in Chinese with English abstract).

Chen, X.H., Yin, A., Gehrels, G.E., Cowgill, E.S., Grove, M., Harrison, T.M., and Wang, X.F., 2003. Two phases of Mesozoic north–south extension in the eastern Altyn Tagh range, northern Tibetan Plateau. Tectonics, 22(5): 1053.

De Waal, S.A., Xu, Z.H., Li, C.S., and Mouri, H., 2004. Emplacement of viscous mushes in the Jinchuan ultramafic intrusion, western China. The Canadian Mineralogist, 42(2): 371–392.

Deng, J., Yuan, W.M., Carranza, E.J.M., Yang, L.Q., Wang, C.M., Yang, L.Y., and Hao, N.N, 2014. Geochronology and thermochronometry of the Jiapigou gold belt, northeastern China: New evidence for multiple episodes of mineralization. Journal of Asian Earth Sciences, 89: 10–27.

Dewey, J.F., Shackleton, R.M., Chang, C.F., and Sun, Y.Y., 1988. The tectonic evolution of the Tibetan Plateau. Philosophical Transactions of the Royal Society A: Mathematical, Physical and Engineering Sciences, 327(1594): 379–413.

Ding, R.X., Zhou, Z.Y., and Wang, W., 2007. Modeling exhumation rates of orogenic belts with low-temperature thermochronological data. Advances in Earth Science, (5): 447–455 (in Chinese with English abstract).

Donelick, R.A., O'Sullivan, P.B., and Ketcham, R.A., 2005. Apatite fission-track analysis. Reviews in Mineralogy and Geochemistry, 58(1): 49–94.

Duan, J., Li, C.S., Qian, Z.Z, and Jiao, J.G., 2015. Geochronological and geochemical constraints on the petrogenesis and tectonic significance of Paleozoic dolerite dykes in the southern margin of Alxa Block, North China Craton. Journal of Asian Earth Sciences, 111: 244–253.

Ehlers, T.A., 2005. Crustal thermal processes and the interpretation of thermochronometer data. Reviews in Mineralogy and Geochemistry, 58(1): 315–350.

England, P., and Molnar, P., 1990. Surface uplift, uplift of rocks, and exhumation of rocks. Geology, 18(12): 1173–1177.

Fan, B.C., Liu, M.Y., He, Z.X., Meng, G.L., Wu, H.H., and Li, L., 2021. Mesozoic–Cenozoic tectonic evolution and uplift in Pamir: Application of fission track thermochronology. Acta Geologica Sinica (English Edition), 95(3): 780–793.

Feng, Y.L., Yuan, W.M., Tian, Y.T., Feng, X., Hao, N.N, Zhang, L.T., Li, Y.H, Liu, Q.S., Wang, X.L., Shi, Z., Zhu, X.Y., Wang, K., and Zhang, A.K., 2017. Preservation and exhumation history of the Harizha–Halongxiuma mining area in the East Kunlun Range, Northeastern Tibetan Plateau, China. Ore Geology Reviews, 90: 1018–1031.

Galbraith, R.F., 1990. The radial plot: Graphical assessment of spread in ages. Nuclear Tracks and Radiation Measurements, 17(3): 207–214.

Galbraith, R.F., and Laslett, G.M., 1993. Statistical models for mixed fission track ages. Nuclear Tracks and Radiation Measurements, 21(4): 459–470.

Gao, H., Hronsky, J., Cao, D.H., Li, R.P., and Zhang, P., 2009. An analysis on the metallogenetic model and ore-control factors of the Jinchuan Cu-Ni-(PGE) magmatic sulfide deposit and its exploration implications. Geology and Exploration, 45 (3): 218–228 (in Chinese with English abstract).

Gao, Y.L., Tang, Z.L., Zhang, M.J., Tian, Y.L., and Xiao, L.Z., 2009. Geochemical characteristics, genesis of a concealed Cu-rich ore body in the Jinchuan deposit, Northwestern China, and its prospecting. Acta Geologica Sinica (English Edition), 83(6): 1085–1100.

George, A.D., Marshallsea, S.J., Wyrwoll, K.H., Chen, J., and Lu, Y.C., 2001. Miocene cooling in the northern Qilian Shan, northeastern margin of the Tibetan Plateau, revealed by apatite fission-track and vitrinite-reflectance analysis. Geology, 29: 939–942.

Gleadow, A.J.W., 1981. Fission-track dating methods: What are the real alternatives? Nuclear Tracks, 5(1–2): 3–14.

Gleadow, A.W., and Duddy, I.R., 1981. A natural long-term track annealing experiment for apatite. Nuclear Tracks, 5: 169 –174.

Gong, J.H., Zhang, J.X., Yu, S.Y., Li, H.K., and Hou, K.J., 2012. Ca. 2.5 Ga TTG rocks in the western Alxa Block and their implications. Chinese Science Bulletin, 57(31): 4064–4076.

Gunnell, Y., Gallagher, K., Carter, A., Widdowson, M., and Hurford, A. J., 2003. Denudation history of the continental margin of western peninsular India since the early Mesozoic—Reconciling apatite fission-track data with geomorphology. Earth and Planetary Science Letters, 215(1): 187–201.

Hasebe, N., Barbarand, J., Jarvis, K., Carter, A., and Hurford, A. J., 2004. Apatite fission-track chronometry using laser ablation ICP-MS. Chemical Geology, 207(3–4): 135–145.

Jiao, J.G., Han, F., Zhao, L.D., Duan, J., and Wang, M.X., 2019. Magnetite geochemistry of the Jinchuan Ni-Cu-PGE deposit, NW China: Implication for its ore-forming processes. Minerals, 9(10): 593.

Kang, H., Chen, Y.L., Li, D.P., Bao, C., Chen, Y.W., Xue, H., and Li, S., 2018. Detrital zircon record of rivers' sediments in the North Qilian Orogenic Belt: Implications of the tectonic evolution of the northeastern Tibetan Plateau. Geological Journal, 54(4): 2208–2228.

Kesler, S.E., and Wilkinson, B.H., 2006. The role of exhumation in the temporal distribution of ore deposits. Economic Geology, 101(5): 919–922.

Ketcham, R.A., 2005. Forward and inverse modeling of low-temperature thermochronometry data. Reviews in Mineralogy and Geochemistry, 58(1): 275–314.

Ketcham, R.A., Carter, A., Donelick, R.A., Barbarand, J., and Hurford, A.J., 2007. Improved measurement of fission-track annealing in apatite using c-axis projection. American Mineralogist, 92(5–6): 789–798.

Ketcham, R.A., Donelick, R.A., and Donelick, M.B., 2000. Aftsolve: A program for multi-kinetic modeling of apatite fission-track data. Geological Materials Research, 88(5–6): 929.

Li, B., Chen, X.H., Zuza, A.V., Hu, D.G., Ding, W.C., Huang, P.H., and Xu, S.L., 2018. Cenozoic cooling history of the North Qilian Shan, northern Tibetan Plateau, and the initiation of the Haiyuan fault: Constraints from apatite and zircon-fission track thermochronology. Tectonophysics, 751: 109–124.

Li, J.Y., Wang, W.T., Wang, Y., Zhang, P.Z., and Wang, Y., 2020. The northward growth of the northeastern Tibetan Plateau in late Cenozoic: Implications from apatite (U-Th)/He ages of Longshou shan. Seismology and Geology, 42(2): 472–491.

Li, X.H., Su, L., Chung, S.L., Li, Z.X., Liu, Y., Song, B., and Liu, D.Y., 2005. Formation of the Jinchuan ultramafic intrusion and the world's third largest Ni-Cu sulfide deposit: Associated with the ~825 Ma south China mantle plume? Geochemistry, Geophysics, Geosystems, 6(11): 1029–1044.

Li, Z.X., Li, X.H., Kinny, P.D., and Wang, J., 1999. The breakup of Rodinia: Did it start with a mantle plume beneath South China? Earth and Planetary Science Letters, 173(3): 171–181.

Lin, X.B., Chen, H.L., Wyrwoll, K.H., Batt, G.E., Liao, L., and Xiao, J., 2011. The uplift history of the Haiyuan-Liupan Shan Region northeast of the present Tibetan Plateau: Integrated constraint from stratigraphy and thermochronology. The Journal of Geology, 119(4): 372–393.

Liu, J., Yu, Q., Wang, M., Jiao, J.G., Chen, C.F., and Ma, Y.F., 2022. Apatite fission track constraints on the late Mesozoic uplifting and cooling events of the Jinchuan Cu-Ni Sulfide deposit. Geotectonica et Metallogenia (in Chinese with English abstract). http://kns.cnki.net/kcms/detail/44.1595.P.20220111.1103.002.html

Liu, J.N., Yin, C.Q., Zhang, J., Qian, J.H., Li, S., Xu, K.Y., Wu, S.J., and Xia, Y.F., 2020. Tectonic evolution of the Alxa Block and its affinity: Evidence from the U-Pb geochronology and Lu-Hf isotopes of detrital zircons from the Longshoushan Belt. Precambrian Research, 344: 105733.

Liu, W.H., Spier, C., Niu, Y.B., Liu, X.D., Yan, J., Wang, K.X., and Pan, J.Y., 2021. Magma mixing in the genesis of the Qingshanbao granitoids in the Longshoushan area: Implications for the tectonic evolution of the North Qilian orogenic belt. Geological Journal, 56(9): 4594–4617.

Liu, X.L., Yang, Z.M., Lu, Y.X., Zhang, N., Dong, L.L., Jiao, Q.Q., Chen, J.H., and Yang, F.C., 2021. Exhumation of the Late Cretaceous ore-forming porphyries in Zhongdian area, Northwestern Yunnan: Evidence from fission track analysis. Acta Geologica Sinica (English Edition), 95(5): 1786–1787.

Lu, L.S., Li, H.B., Yang, X.N., Liu, J., Mao, B., and Li, B.L., 2018. Neoproterozoic magmatic Ni-Cu-(PGE) sulfide deposits related to the assembly and breakup of the Rodinia supercontinent in China: An overview. Ore Geology Reviews, 99: 282–302.

Ma, G.Y., Gao, J.P., Du, D.D., Bai, Y.B., and Pan, X., 2014. Uplift destruction after mineralization in the Jinchuan copper-nickel deposit: Evidence from thermochronology. World Geology, 33(3): 581–590 (in Chinese with English abstract).

Mao, X.C., Li, L.J., Liu, Z.K., Zeng, R.Y., Dick, J., Yue, B., and Ai, Q.X., 2019. Multiple magma conduits model of the Jinchuan Ni-Cu-(PGE) deposit, Northwestern China: Constraints from the geochemistry of Platinum-Group elements. Minerals, 9(3): 187.

McInnes, B.I.A., Evans, N.J., Fu, F.Q., and Garwin, S., 2005. Application of thermochronology to hydrothermal ore deposits. Reviews in Mineralogy and Geochemistry, 58: 467–498.

Meert, J.G., and Torsvik, T.H., 2003. The making and unmaking of a supercontinent: Rodinia revisited. Tectonophysics, 375: 261–288.

Naldrett, A.J., 1997. Key factors in the genesis of Noril'sk, Sudbury, Jinchuan, Voisey's Bay and other world-class Ni-Cu -PGE deposits: Implications for exploration. Australian Journal of Earth Sciences, 44(3): 283–315.

Naldrett, A.J., 1999. World-class Ni-Cu-PGE deposits: Key factors in their genesis. Mineralium Deposita, 34: 227–240.

Reiners, P.W., and Brandon, M.T., 2006. Using thermochronology to understand orogenic erosion. Annual Review of Earth and Planetary Sciences, 34(1): 419–466.

Ren, Z.L., 1998. Comparative research on tectonical thermal history of sedimentary basins in North China (M.Sc. Thesis). Xi'an: Northwest University, 119–144.

Shi, Y.J., Zhang, C.W., and Cun, S.C., 1995. The discovery of the Longshoushan overthrust structure and its geological significance. Chinese Science Bulletin, (9): 812–813 (in Chinese).

Song, C.H., Meng, Q.Q., Xia, W.M., Xu, L., Miao, Y.F., Yang, Y.B., and Hu, S.H., 2009. The Eogene surface texture of quartz sand and paleoclimatic change in northern margin of Tibetan Plateau. Acta Sedimentologica Sinica, 27(01): 94–103 (in Chinese with English abstract).

Song, X.Y., Keays, R.R, Zhou, M.F., Qi, L., Ihlenfeld, C., and Xiao, J.F., 2009. Siderophile and chalcophile elemental constraints on the origin of the Jinchuan Ni-Cu-(PGE) sulfide deposit, NW China. Geochimica et Cosmochimica Acta, 73 (2): 404–424.

Sun, Y., Chen, Z., Boone, S. C., Zhong, F., and Tao, W., 2021. Exhumation history and preservation of the Changjiang uranium ore field, South China, revealed by (U-Th)/He and fission track thermochronology. Ore Geology Reviews, 133: 104101.

Tang, Q.Y., Li, C.S., Zhang, M.J., Ripley, E.M., and Wang, Q.L., 2014. Detrital zircon constraint on the timing of amalgamation between Alxa and Ordos, with exploration implications for Jinchuan-type Ni-Cu ore deposit in China. Precambrian Research, 255(S1): 748–755.

Tang, Z.L., Yang, J.D., Xu, X.C., and Li, W.Y., 1992. Sm-Nd dating of the Jinchuan ultramafic intrusion, Gansu, China. Chinese Science Bulletin, (23): 1988–1990.

Tang, Z.L., and Bai, Y.L., 2000. The geotectonic setting of the large and superlarge mineral deposits in the southwest margin of the North China paleoplate. Gansu Geology, (1): 1–15 (in Chinese with English abstract).

Tian, X.S., Yang, J., Liu, X.D., and Di, P.F., 2016. Mesozoic–Cenozoic lifting and cooling process of the Jinchuan Copper-Nickel sulfide deposit: Evidence from the fission-track method. Gansu Geology, 25(2): 50–55+75 (in Chinese with English abstract).

Vermeesch, P., 2009. RadialPlotter: A Java application for fission track, luminescence and other radial plots. Radiation Measurements, 44(4): 409–410.

Wang, J.P., Zhai, Y.S., Liu, J.J., Liu, Z.J., and Liu, J., 2008. A new approach to post-ore change and preservation of ore deposits: Fission track analysis. Advances in Earth Science, (4): 421–427 (in Chinese with English abstract).

Wang, W.T., Zhang, P.Z., Zheng, D.W., and Pang, J.Z., 2014. Late Cenozoic tectonic deformation of the Haiyuan fault zone in the northeastern margin of the Tibetan Plateau. Earth Science Frontiers, 21(4): 266–274 (in Chinese with English abstract).

Wu, C., Zuza, A.V., Li, J., Haproff, P.J., Yin, A., Chen, X.H., Ding, L., and Li, B., 2021. Late Mesozoic–Cenozoic cooling history of the northeastern Tibetan Plateau and its foreland, derived from low-temperature thermochronology. Geological Society of America Bulletin, 133(11–12): 2393–2417.

Wu, Z.Y., Guo, Y.S., and Sun, S.H., 1992. Temperature-pressure calculation of the Jinchuan copper and nickel sulfide deposit and discussion on the minerogenetic mechanism. Mineralogy and Petrology, (1): 89–95 (in Chinese with English abstract).

Wyborn, L.A.I., Heinrich, C.A., and Jauqes, A.L., 1994. Australian Proterozoic mineral systems: Essential ingredients and mappable criteria. In: Hallenstein, P.C. (ed.) Australian Mining Looks North—The Challenges and Choices, vol 5. Australian Institute of Mining and Metallurgy Publication Series, 109–115.

Xiang, F., Zhang, D.Y., Chen, K., and Feng, Q., 2015. Early Cretaceous paleoclimate characteristics of China: Clues from continental climate-indicative sediments. Acta Geologica Sinica (English Edition), 89(4): 1307–1318.

Xiao, W.Z., Lai, J.Q., Dick, J.M., Mao, X.C., Chen, Y., Ou, Q., Xie, F.Q., Zeng, R.Y., and Li, S.Z., 2018. Tectonic affinity and evolution of the Alxa Block during the Neoproterozoic: Constraints from zircon U-Pb dating, trace elements, and Hf isotopic composition. Geological Journal, 54(6): 3700–3719.

Xie, G.H., Wang, Y.L., Fan, C.Y., Zhang, C.J., and Zheng, R., 1998. Genetic mechanisms of the Jinchuan ultramafic intrusion and associated superlarge sulfide deposit, Northwest China. Science in China (Series D: Earth Sciences), (S1): 65–73.

Yang, G., Du, A.D., Lu, J.R., Qu, W.J., and Chen, J.F., 2005. Re-Os (ICP-MS) dating of the massive sulfide ores from the Jinchuan Ni-Cu-PGE deposit. Science China-Earth Sciences, 48(10): 1672–1677.

Yang, S.H., Qu, W.J., Tian, Y.L., Chen, J.F., Yang, G., and Du, A.D., 2008. Origin of the inconsistent apparent Re-Os ages of the Jinchuan Ni-Cu sulfide ore deposit, China: Post-segregation diffusion of Os. Chemical Geology, 247(3–4): 401–418.

Yang, X.Y., Yin, J.Y., Xiao, W.J., Chen, W., Chen, Y.L., Sun, J.B., Zhang, B., and Wang, Y.M., 2021. Late Mesozoic and Cenozoic tectono-thermal history of the Nadanhada region, NE China: Evidence from combined fission track and (U-Th)/He thermochronology. Acta Geologica Sinica, 95(12): 3660–3675 (in Chinese with English abstract).

Yang, Z.X., Peng, L.G., Dong, X.Y., Hou, S.J., Gong, Z.C., and An, S.Y., 1991. The characteristics and geological significance of magmatic inclusions in the Jinchuan copper-nickel-bearing ultrabasic intrusion, Gansu Province. Geological Review, 37(1): 70–79+98 (in Chinese with English abstract).

Yu, C.D., Wang, K.X., Liu, X.D., Cuney, M., Pan, J.Y., Wang, G., Zhang, L., and Zhang, J., 2020. Uranium mineralogical and chemical features of the Na-metasomatic type uranium deposit in the Longshoushan Metallogenic Belt, Northwestern China. Minerals, 10(4): 335.

Yu, Q., Ren, Z.L., Wang, B.J, Zheng, W.B., and Tao, N., 2018. Geothermal field and deep thermal structure of the Tianshan–Altun region. Geological Journal, 53(2): 237–251.

Yu, Q., Ren, Z.L, Li, R.X., Tao, N., Qi, K., Jiang, C., and Wang, B.J., 2019. Meso-Cenozoic tectonothermal history of Permian strata, southwestern Weibei uplift: Insights from thermochronology and geothermometry. Acta Geologica Sinica (English Edition), 93(6): 1647–1661.

Yu, Q., Ren, Z.L., Li, R.X., Chung, L., Tao, N., Cui, J.P., Wang,

B.J., Qi, K., and Khaleda, A., 2021. Cooling history of the southwestern Ordos Basin (northern China) since Late Jurassic: Insights from thermochronology and geothermometry. Journal of Asian Earth Science, 219: 104895.

Yu, Q., Ren, Z.L., Li, R.X., Chung, L., Tao, N., Lei, W.S., Wang, B.J., Wu, X.L., Qin, X.L., and Lei, X.H., 2022. Different burial-cooling history of Triassic strata between the western Weibei Uplift and the northwestern Weihe Basin in northwest China. Journal of Earth Science (in Chinese with English abstract). http://kns.cnki.net/kcms/detail/42.1788.P.20210223.1240.002.html

Yuan, D.Y., Ge, W.P., Chen, Z.W., Li, C.Y., Wang, Z.C., Zhang, H.P., Zhang, P.Z., Zheng, D.W., Zheng, W.J., Craddock, W.H., Dayem, K.E., Duvall, A.R., Hough, B.G., Lease, R.O., Champagnac, J.D., Burbank, D.W., Clark, M.K., Farley, K.A., Garzione, C.N., Kirby, E., Molnar, P., and Roe, G.H., 2013. The growth of northeastern Tibet and its relevance to large-scale continental geodynamics: A review of recent studies. Tectonics, 32(5): 1358–1370.

Yuan, W.M., Yang, Z.Q., Zhang, Z.C., and Deng, J., 2011. The uplifting and denudation of main Huangshan Mountains, Anhui Province, China. Science China (Earth Sciences), 54 (8): 1168–1176.

Yuan, W.M., 2016. Thermochronological method of revealing conservation and changes of mineral deposits. Acta Petrologica Sinica, 32(8): 2571–2578 (in Chinese with English abstract).

Zeitler, P.K., Tahirkheli, R.A.K., Naeser, C.W., and Johnson, N.M., 1982. Unroofing history of a suture zone in the Himalaya of Pakistan by means of fission-track annealing ages. Earth and Planetary Science Letters, 57(1): 227–240.

Zeng, R.Y., Lai, J.Q., Mao, X.C., and Tao, J.J., 2013. Evolution of fault system and its controlling on Jinchuan Cu-Ni (PGE) sulfide deposit. The Chinese Journal of Nonferrous Metals, 23 (9): 2574–2583.

Zeng, R.Y., Lai, J.Q., Mao, X.C., Bin, L., Ju, P.J., and Tao, S.L, 2016. Geochemistry, zircon U-Pb dating and Hf isotopes composition of Paleozoic granitoids in Jinchuan, NW China: Constraints on their petrogenesis, source characteristics and tectonic implications. Journal of Asian Earth Sciences, 121: 20–33.

Zhai, Y.S., Deng, J., and Peng, R.M., 2000. Research contents and methods for post-ore changes, modifications and preservation. Earth Science, (4): 340–345 (in Chinese with English abstract).

Zhang, X.H., 1992. Basic characteristics and evolution history of Longshoushan paleorift zone. Northwestern Geology, (1): 6–13 (in Chinese).

Zhang, Z.Q., Du, A.D., Tang, S.H., Lu, J.R., Wang, J.H., and Yang, G., 2004. Age of the Jinchuan copper-nickel deposit and isotopic geochemical features of its source. Acta Geologica Sinica, (3): 359–365 (in Chinese with English abstract).

Zhang, J., Li, J.Y., Li, Y.F., and Ma, Z.J., 2009. How did the Alxa Block respond to the Indo-Eurasian collision? International Journal of Earth Sciences, 98(6): 1511–1527.

Zhang, B.H., Zhang, J., Wang, Y.N., Zhao, H., and Li, Y.F., 2017. Late Mesozoic–Cenozoic exhumation of the Northern Hexi Corridor: Constrained by apatite fission track ages of the Longshoushan. Acta Geologica Sinica (English Edition), 91 (5): 1624–1643.

Zhang, L.Q., Zhang, H.F., Zhang, S.S., Xiong, Z.L., Luo, B.J., Yang, H., Pan, F.B., Zhou, X.C., Xu, W.C., and Guo, L., 2017. Lithospheric delamination in post-collisional setting: Evidence from intrusive magmatism from the North Qilian orogen to southern margin of the Alxa block, NW China. Lithos, 288–289: 20–34.

Zhang, M.J., Kamo, S.L., Li, C.S., Hu, P.Q., and Ripley, E.M., 2010. Precise U-Pb zircon-baddeleyite age of the Jinchuan sulfide ore-bearing ultramafic intrusion, western China. Mineralium Deposita, 45(1): 3–9.

Zhao, R.S., Zhou, Z.H., Mao. J.H., and Zhou, Z.X., 1994. Plate tectonic units and tectonic evolution in Gansu. Geological Bulletin of China, (1): 28–36 (in Chinese with English abstract).

Zhao, G.C., and Cawood, P.A., 2021. Precambrian geology of China. Precambrian Research, 222: 13–54.

Zhao, Y., Liu, S.A., Xue, C., and Li, M.L., 2022. Copper isotope evidence for a Cu-rich mantle source of the world-class Jinchuan magmatic Ni-Cu deposit. American Mineralogist: Journal of Earth and Planetary Materials, 107(4): 673–683.

Zheng, D.W., Wang, W.T., Wan, J.L., Yuan, D.Y., Liu, C.R., Zheng, W.J., Zhang, H.P., Pang, J.Z., and Zhang, P.Z, 2017. Progressive northward growth of the northern Qilian Shan–Hexi Corridor (northeastern Tibet) during the Cenozoic. Lithosphere, 9(3): 408–16.

Zhou, Z.Y., and Donelick, R.A., 2001. Multikinetic modeling for time-temperature history based on apatite fission track data. Petroleum Geology and Experiment, (1): 97–102 (in Chinese with English abstract).

Zhu, W.B., Zhang, Z.Y., Shu, L.S., Wan, J.L., Lu, H.F., Wan, S.L., Yang, W., and Su, J.B., 2007. Uplift and exhumation history of the Precambrian basement, Northern Tarim: Evidence from apatite fission track data. Acta Petrologica Sinica, 23(7): 1671–1682 (in Chinese with English abstract).

Zhuang, G.S., Johnstone, S., Hourigan, J., Lippert, P., Ritts, B., Robinson, A., and Sobel, E.R., 2018. Understanding the geologic evolution of Northern Tibetan Plateau with multiple thermochronometers. Gondwana Research, 58: 195–210.

About the first author

LEI Xianghe, male, born in 1997 in Pingliang, Gansu Province; graduated from Southwest Petroleum University; master of School of Earth Science and Resources, Chang'an University. He is currently engaged in apatite fission track thermochronology to restore the thermal history of sedimentary basins. E-mail: 2046649399@qq.com.

About the corresponding author

YU Qiang, male, born in 1983 in Xi'an, Shaanxi Province; doctor; graduated from Northwest University; associate professor, School of Earth Science and Resources, Chang'an University, Head of the Department of Petroleum. He is currently engaged in the recovery of tectonothermal evolutionary history and low-temperature thermochronology. E-mail: yuqiang@chd.edu.cn.